

Forced response and internal variability of summer climate over western North America

著者	KAMAE Youichi, SHIOGAMA Hideo, IMADA Yukiko, MORI Masato, ARAKAWA Osamu, MIZUTA Ryo, YOSHIDA Kohei, TAKAHASHI Chiharu, ARAI Miki, ISHII Masayoshi, WATANABE Masahiro, KIMOTO Masahide, XIE Shang-Ping, UEDA Hiroaki
journal or publication title	Climate Dynamics
volume	49
number	1-2
page range	403-417
year	2017-01
権利	Authors may self-archive the author ' s accepted manuscript of their articles on their own websites. Authors may also deposit this version of the article in any repository, provided it is only made publicly available 12 months after official publication or later. He/ she may not use the publisher's version (the final article), which is posted on SpringerLink and other Springer websites, for the purpose of self-archiving or deposit. Furthermore, the author may only post his/her version provided acknowledgement is given to the original source of publication and a link is inserted to the published article on Springer's website. The link must be provided by inserting the DOI number of the article in the following sentence: " The final publication is available at Springer via http://dx.doi.org/10.1007/s00382-016-3350-x " .
URL	http://hdl.handle.net/2241/00147216

1 **Forced response and internal variability of summer climate over** 2 **western North America**

3
4 Youichi Kamae^{1,2*}, Hideo Shiogama³, Yukiko Imada⁴, Masato Mori⁵, Osamu Arakawa¹, Ryo Mizuta⁴, Kohei
5 Yoshida⁴, Chiharu Takahashi⁵, Miki Arai⁵, Masayoshi Ishii⁴, Masahiro Watanabe⁵, Masahide Kimoto⁵,
6 Shang-Ping Xie², and Hiroaki Ueda¹

7
8 ¹Faculty of Life and Environmental Sciences, University of Tsukuba, Tsukuba, Ibaraki, Japan

9 ²Scripps Institution of Oceanography, University of California San Diego, La Jolla, California, USA

10 ³Center for Global Environmental Research, National Institute for Environmental Studies, Tsukuba, Ibaraki,
11 Japan

12 ⁴Meteorological Research Institute, Tsukuba, Ibaraki, Japan

13 ⁵Atmosphere and Ocean Research Institute, University of Tokyo, Kashiwa, Chiba, Japan

14
15 Submitted to *Climate Dynamics*

16
17
18 *Corresponding author: Youichi Kamae, Faculty of Life and Environmental Sciences, University of Tsukuba,
19 1-1-1 Tennoudai, Tsukuba, Ibaraki 305-8506, Japan (kamae.yoichi.fw@u.tsukuba.ac.jp), Tel.:
20 +81-29-853-4757 Fax: +81-29-853-6709

23 **Abstract**

24 Over the past decade, anomalously hot summers and persistent droughts frequented over the western
25 United States (wUS), the condition similar to the 1950s and 1960s. While atmospheric internal variability is
26 important for mid-latitude interannual climate variability, it has been suggested that anthropogenic external
27 forcing and multidecadal modes of variability in sea surface temperature (SST), namely, the Pacific Decadal
28 Oscillation (PDO) and Atlantic Multidecadal Oscillation (AMO), also affect the occurrence of droughts and hot
29 summers. In this study, 100-member ensemble simulations for 1951–2010 by an atmospheric general circulation
30 model (AGCM) were used to explore relative contributions of anthropogenic warming, atmospheric internal
31 variability, and atmospheric response to PDO and AMO to the decadal anomalies over the wUS. By comparing
32 historical and sensitivity simulations driven by observed sea surface temperature, sea ice, historical forcing
33 agents, and non-warming counterfactual climate forcing, we found that large portions of recent increases in mean
34 temperature and frequency of hot summers (66% and 82%) over the wUS can be attributed to the anthropogenic
35 global warming. In contrast, multidecadal change in the wUS precipitation is explained by a combination of the
36 negative PDO and the positive AMO after the 2000s. Diagnostics using a linear baroclinic model indicate that
37 AMO- and PDO-related diabatic heating anomalies over the tropics contribute to the anomalous atmospheric
38 circulation associated with the droughts and hot summers over wUS on multidecadal timescale. Those anomalies
39 are not robust during the periods when PDO and AMO are in phase. The prolonged PDO–AMO antiphase period
40 since the late 20th century resulted in the substantial component of multidecadal anomalies in temperature and
41 precipitation over the wUS.

42 **Keywords:** Global warming hiatus, PDO, AMO, hot summers, linear baroclinic model

43 **1. Introduction**

44 Since the late 20th century, mean temperature and frequency of warm extremes have both remarkably
45 increased over land (e.g. Hansen et al. 2012; Perkins et al. 2012). Anthropogenic influences including
46 human-induced greenhouse gases emissions play an essential role in the observed climate change during the
47 recent six decades (e.g. Jones et al. 2013; IPCC 2013). In addition, intrinsic variability in the climate system also
48 influences decadal-to-centennial climate trends particularly during the winter season (Hawkins and Sutton 2009;
49 Deser et al. 2012). Since the end of the 20th century, substantial decadal-to-multidecadal variations (DMV) in
50 the rate of global-mean temperature increase have been observed. Particularly, temperature and precipitation
51 trends during these decades exhibit substantial regionality associated with anomalous atmospheric circulations,
52 suggesting an important role of natural climate variability (e.g. Horling et al. 2010; Wang et al. 2013; Kamae et
53 al. 2014a, b, 2015; Ueda et al. 2015; Gu et al. 2016; Zhou and Wu 2016). The literature suggested an importance
54 of sea surface temperature (SST) DMV over the Indian (Luo et al. 2012), Atlantic (McGregor et al. 2014; Li et al.
55 2016), and Pacific (Kosaka and Xie 2013; England et al. 2014; Watanabe et al. 2014) Oceans. Anomalous
56 convective activity over the tropics associated with the SST variations can influence mid-latitude climate
57 variations via changing atmospheric circulations (Trenberth et al. 2014; Ding et al. 2014; Ueda et al. 2015).

58 Climate extremes including multi-year droughts, pluvials and warm extremes have been a recurrent
59 feature of the western United States (wUS; e.g. Cook et al. 2007). Since around the year 2000, extreme hot
60 summers and persistent droughts were frequently observed over the wUS (e.g. Seager and Hoerling 2014;
61 Shiogama et al. 2014; Delworth et al. 2015) despite a slowdown of global-mean surface warming (e.g. Kosaka

62 and Xie 2013; Fyfe et al. 2016; detailed in Sects. 3.1 and 3.2). Droughts and heat waves are coupled via
63 land-atmosphere interaction over semi-arid regions (Mueller and Seneviratne 2012). Less precipitation over the
64 wUS tends to be associated with cool SST over the tropical eastern Pacific (e.g. Ting and Wang 1997; Wang and
65 Schubert 2014). In addition to the El Niño Southern Oscillation (ENSO), Pacific SST DMVs associated with the
66 Interdecadal Pacific Oscillation (IPO) or Pacific Decadal Oscillation (PDO; Mantua et al. 1997; Power et al.
67 1999; Deser et al. 2004; Newman et al. 2016) also contribute to precipitation variability (Seager et al. 2005;
68 Meehl and Hu 2006; Cook et al. 2011; Dai 2013; Seager and Hoerling 2014; Burgman and Jang 2015; Delworth
69 et al. 2015). Other analytical and numerical studies, on the other hand, suggested the importance of Atlantic SST
70 anomaly on the wUS precipitation variation (Sutton and Hodson 2005, 2007; Kushnir et al. 2010; Cook et al.
71 2011; Feng et al. 2011). Kushnir et al. (2010) revealed that the atmospheric response to deep-tropospheric
72 diabatic heating associated with the warm Atlantic SST contributes to a reduction of precipitation over central
73 North America via changing atmospheric circulations.

74 Both the anthropogenic influence and the naturally-generated climate variations affect mean SAT,
75 precipitation and climate extremes over the middle latitudes including the wUS (e.g. Meehl et al. 2007; Jones et
76 al. 2013; Shiogama et al. 2014; Diffenbaugh et al. 2015; Xie et al. 2015). However, the forced component of the
77 climate variations is difficult to detect due to the predominant atmospheric internal variability in the middle
78 latitudes. Kamae et al. (2014a) decomposed historical variations of warm extremes over land into anthropogenic
79 influence and naturally-generated climate variation by using 10-member ensemble atmospheric general
80 circulation model (AGCM) simulations. The relative importance of atmospheric internal variability is

81 predominant in the variation of the frequency of hot summers over the middle latitudes (Fig. 2c in Kamae et al.
82 2014a). By using results of ensemble AGCM simulations prescribed with observed SST, contributions of
83 anthropogenic forcing and naturally-generated climate variability to observed climate anomalies including the
84 warm and dry wUS climate in the 2000s can be examined. In addition, coarser resolution models are not well
85 suited for reproducing regional atmospheric circulation and seasonal precipitation patterns over the wUS because
86 the regional climate system is associated with complex terrain (Langford et al. 2014; Brewer and Mass 2016). In
87 this study, we examine the relative importance of anthropogenic influence, atmospheric internal variability, and
88 atmospheric response to naturally-generated SST variation in the historical variations over land including the
89 wUS on different timescales. For this purpose, we use a high-resolution, 100-member ensemble AGCM
90 simulation for 1951–2010. Using the large ensemble enables to examine relative importance of forced
91 atmospheric variation to SST variability modes compared with internal atmospheric variability. We focus on
92 mean temperature, frequency of hot summers, and precipitation over land during boreal summer. Section 2
93 describes the data and methods including observations, reanalysis and modeled data analyzed in this study.
94 Section 3 presents the historical climate variations over the Northern Hemisphere land areas and the wUS. We
95 also quantify the anthropogenic influence the wUS climate variation. Section 4 examines roles of DMV in SST
96 over the Pacific and Atlantic in the wUS climate variations. Section 5 evaluates relative contributions of forced
97 atmospheric response and internal variability to the historical climate variation on different timescales. In Sect. 6,
98 we present a summary and discussion.

99

100 **2. Data and methods**

101 **2.1. Observations and reanalysis**

102 We used CRU TS v3.23 dataset (Harris et al. 2014) as reference data representing the observed climate
103 state for 1901–2010. We used monthly mean surface air temperature (SAT) data in $0.5^\circ \times 0.5^\circ$ spatial resolution
104 to examine historical variations of mean temperature and frequency of hot summers over land (Sect. 2.4). We
105 mainly used SAT for 1951–2010 to compare with modeled climate variation (Sect. 2.2). For examining surface
106 and three dimensional atmospheric states for 1958–2010, the Japanese 55-year Reanalysis (JRA-55; Kobayashi
107 et al. 2015) was used. Data in $0.5^\circ \times 0.5^\circ$ and $1.25^\circ \times 1.25^\circ$ spatial resolutions were used in the analyses for
108 surface and three dimensional variables, respectively. For global precipitation (including over the ocean), the
109 dataset of the Global Precipitation Climatology Project (GPCP; version 2.2; Alder et al. 2003) was used to
110 examine multidecadal precipitation variability during 1979–2010. Historical variations in SST were examined by
111 using HadISST (Rayner et al. 2003) at $1.0^\circ \times 1.0^\circ$ spatial resolution.

112

113 **2.2. Large ensemble in an AGCM**

114 In this study, large-ensemble historical simulations with a high-resolution AGCM (Mizuta et al. 2016)
115 were used to examine SST- and emission-forced climate response and atmospheric internal variability for 1951–
116 2010. The Meteorological Research Institute Atmospheric General Circulation Model (MRI-AGCM) version 3.2
117 (Mizuta et al. 2012) was used for 100-member ensemble historical simulations. The model was run at a
118 horizontal resolution of TL319 (equivalent to 60-km mesh) with 64 vertical layers (Murakami et al. 2012). For

119 the ensemble historical simulations (hereafter ALL run), the AGCM was driven by observation-based SST and
120 sea ice (Hirahara et al. 2014) and historical radiative forcing agents (greenhouse gases, aerosols, and ozone) for
121 1951–2010. The ozone concentration was based on results of Reference Simulation 2 for the Chemistry Climate
122 Models Validation (Eyring et al. 2005) using the MRI Chemical Transport Model (Shibata et al. 2005). The
123 aerosols were derived from the results of a present-day experiment using a prototype version of MRI Earth
124 System Model version 1 (MRI-ESM1; Yukimoto et al. 2011), in which the historical emission flux and the
125 surface emission inventories were prescribed. 5-year running mean of the ozone and aerosols were incorporated
126 into the AGCM. To develop 100-member ensemble, SST perturbations based on SST analysis error (Hirahara et
127 al. 2014) were added to the observed SST to account for uncertainties. The perturbations consist of Empirical
128 Orthogonal Functions (EOFs) of the interannual variations (IAV) of the SST analysis. The amplitude of the
129 perturbation is set to be 30% of the standard deviation of the interannual SST variability. Spread in climate
130 response due to the perturbed SST is comparable to that due to initial condition perturbations (Mizuta et al.
131 2016). Sea ice concentration was derived from a quadratic equation on sea-ice-SST relationship (Hirahara et al.
132 2014). By using the 100-member ensemble, the ensemble mean and the deviation of each member from the
133 ensemble mean can be regarded as approximations of forced atmospheric response and internal variability,
134 respectively (Sect. 5). Note that the ensemble mean is also affected by internal variability modes in the
135 atmosphere-ocean coupled system (e.g. PDO).

136 In order to decompose anthropogenic warming and naturally-generated climate variations, 100-member
137 non-warming simulations (hereafter NW run) were conducted. Greenhouse gases were fixed at the level of 1850

138 while ozone was fixed at the level of 1960 in MRI-ESM1 simulation. Sulfate, black carbon, and organic carbon
139 were fixed at climatology of the pre-industrial simulation. Other prescribed aerosols including soil and sea salt
140 particles were identical to the ALL run. In the NW run, the EOF1 mode of SST during 1951–2010 (Hirahara et al.
141 2014), which approximately present the linear trend pattern, was removed from the prescribed SST. Here the
142 anthropogenic influence is assumed to be dominant for the linear trend pattern subtracted from the prescribed
143 SST. Note that effects of low-frequency natural climate fluctuations could be reduced by subtracting the linear
144 trends. However, effects of PDO and AMO are almost not removed because both of the two do not show
145 monotonic trends for this period (see Sect. 3.2). Further discussion on the decomposition method can be found in
146 Christidis and Stott (2014) and Shiogama et al. (2014, 2016). The SST perturbation identical to the ALL run was
147 added to the detrended SST. More details on this dataset called Database for Probabilistic Description of Future
148 Climate Change (d4PDF), including experimental setup of the ALL and NW runs, general representation of
149 climatological spatial patterns and historical variation of the current climate, can be found in Mizuta et al. (2016)
150 and Shiogama et al. (2016).

151

152 **2.3. Linear baroclinic model**

153 To diagnose the atmospheric circulation response to specified convective heating associated with DMV
154 over the tropics, we used a linear baroclinic model (LBM; Watanabe and Kimoto 2000) based on primitive
155 equation linearized around the observed June-July-August (JJA) mean atmospheric state as represented by
156 NCEP/NCAR reanalysis. The model used is a version with T42 resolution in the horizontal and 20 sigma levels

157 in the vertical. The model was forced by anomalous diabatic heating in the tropical atmosphere. Experimental
158 setups including imposed diabatic heating are described in Sect. 4.2.

159

160 **2.4. Definition of hot summers**

161 In this study, hot summers were defined by using climatology and two standard deviations of
162 monthly-mean SAT (Hansen et al. 2012, Kamae et al. 2014a). First, long-term variability and linear trend for
163 1958–2010 were extracted from the SAT in each month and at each grid point. Next, climatology and standard
164 deviations were calculated using the period 1958–2010. We define hot summers as those SAT anomalies exceed
165 two standard deviations. The frequency of hot summers in the Northern Hemisphere land areas was calculated by
166 averaging over the area for each month and then averaged during JJA for each year. Previous studies used a
167 shorter period (1951–1980) for calculating climatology and standard deviations (Hansen et al. 2012; Kamae et al.
168 2014a), and the frequency of hot summers can be biased outside the reference period (Zhang et al. 2005; Sippel
169 et al. 2015). We tested the sensitivity of results to different reference periods and confirmed that interannual and
170 multidecadal variations in frequency of hot summers were qualitatively consistent. However, the amplitudes of
171 the fluctuations were generally larger when the shorter reference period was used. In this study, we used 1958–
172 2010 as the reference period to avoid exaggerated estimates of the temperature variations outside the reference
173 period.

174

175 **3. Anthropogenic and natural variability effects**

176 3.1. Global variations

177 In this section, we examine the general reproducibility of historical climate variations in the ALL run by
178 comparing with observations over the Northern Hemisphere land areas during JJA. Figure 1 shows historical
179 variations of SAT and frequency of hot summers in CRU TS v3.23 (1901–2010), JRA-55 (1958–2010), ALL and
180 NW runs (1951–2010). In all the time series, remarkable IAV, DMV, and long-term increasing trends in SAT and
181 frequency of hot summers can be found since the late 20th century. DMV in SAT is characterized by cooling in
182 the early 20th century (found in CRU TS v3.23) and in the 1960s to 1970s and warming in the 1930s to 1940s
183 and substantial warming trend from the 1980s to present, similar to other datasets (Jones et al. 2013; IPCC 2013).
184 The ensemble AGCM simulations since 1951 capture both the IAV and DMV including the recent warming
185 period. The IAV in SAT is similar to the NW run because much of the IAV in the ensemble mean is atmospheric
186 response to the SST variations including ENSO (Kamae et al. 2014a). The recent warming period is largely due
187 to the effect of anthropogenic warming, as indicated by the difference between the ALL and NW runs (Sect. 2.2),
188 with contribution from the naturally-generated DMV (Kamae et al. 2014a; Watanabe et al. 2014). In the 2000s,
189 summertime warm extremes were frequently observed compared with the late 20th century (Fig. 1b; Hansen et al.
190 2012; Kamae et al. 2014a). The Pacific and Atlantic SST DMV (Zhou and Wu 2016) and direct anthropogenic
191 influences (Kamae et al. 2014a) are important for the decadal-scale increase in frequency of hot summers in the
192 early 21st century despite the slowdown of the annual-mean global-mean SAT increase (e.g. Kosaka and Xie
193 2013; Fyfe et al. 2016).

194 Figure 2 shows spatial distributions of anomalies in SAT and frequency of hot summers during 2000–
195 2010 compared with 1978–1999. The averaging periods correspond to different phases of the PDO and AMO
196 (detailed below). Both JRA-55 and CRU TS v3.23 (not shown) exhibit statistically-significant warming over the
197 broad land areas particularly in the mid-latitude Northern Hemisphere (Fig. 2a; Kamae et al. 2014a, b). Although
198 the ensemble mean of the ALL runs (Fig. 2b) also shows a large warming over the middle latitude, it does not
199 reproduce the substantial spatial asymmetry in observations (e.g. cold anomalies over Central Canada and
200 Central Asia and amplified warming over Central and Eastern Europe and East Asia; Fig. 2a), suggesting the
201 importance of internal atmospheric variability and/or the effect of model biases.

202 Over the last decade, the substantial increases in SAT and extremely warm events with persistent drought
203 were found over the wUS (150°W–120°W; 25°N–50°N; black rectangle in Fig. 2), distinct from the eastern US
204 (Fig. 2a, c; Meehl et al. 2012; Sheffield et al. 2013; Perin et al. 2016). The ensemble mean of the AGCM runs
205 can partly capture the warming and increasing warm extremes over the wUS (Fig. 2b, d), suggesting the
206 importance of forced atmospheric response on the multidecadal timescale. In the next section, we focus on IAV
207 and DMV of the wUS summertime climate.

208

209 **3.2. Western US**

210 Figure 3 shows historical variations of SAT, frequency of hot summers and precipitation over the wUS.
211 Large variations can be found on interannual and multidecadal timescales: warm and dry periods in the 1950s,
212 1960s and 2000s and cool and humid periods in the 1980s to 1990s, consistent with previous reports (e.g. Seager

213 et al. 2005; Dai 2013). The model does not reproduce the substantial IAV (e.g. cooling in 2004 and warming in
214 2006; Fig. 3a–c), suggesting the importance of mid-latitude stochastic internal variability in the atmospheric
215 circulation. In contrast, DMV (e.g. the cool 1970s and warm 1950s, 1990s to 2000s and the humid 1980s to
216 1990s and the dry 1950s and 2000s) is found in the ALL run (Fig. 3d–f). Note that the ensemble mean of the
217 AGCM simulations does not reproduce the reduced precipitation in the 1970s relative to the 1960s (Fig. 3f). The
218 DMV which are simulated in the ALL run are also found in the NW run (except the long-term warming trend),
219 suggesting the important contributions from the naturally-generated SST variations. Here differences in decadal
220 time series between ALL and NW runs are found in SAT and frequency of hot summers (ALL run shows lower
221 and higher values than NW run before and after the 1970s, respectively) but are not apparent for precipitation
222 (Fig. 3d–f), suggesting different contributions of naturally-generated DMV to temperature and precipitation. The
223 anomalies averaged for 2000–2010 compared with 1978–1999 are summarized in Table 1. The observed high
224 SAT, frequent hot summers, and reduced precipitation are qualitatively reproduced in the ensemble mean of ALL
225 run and these anomalies are statistically significant. The majority of the warming and increasing frequency of hot
226 summers (66% and 82%) can be attributed to the anthropogenic influence and the remainders (34% and 18%)
227 result from the NW simulation. As for precipitation, naturally-generated variations contribute to 44% of the
228 recent DMV over the wUS. Although dynamic contributions (i.e. related to atmospheric circulation) to the
229 regional DMV (Wallace et al. 2015; see Sect. 4) are important for both precipitation and temperature in the wUS,
230 relative contribution of long-term trend to DMV in precipitation is smaller than that of SAT because
231 temperature-related thermodynamic contribution is limited for precipitation (Fig. 3f; Deser et al. 2012).

232 The wUS DMV in SAT, hot summers and precipitation shown in Fig. 3 correspond well with PDO and
233 AMO. Figure 3g shows 11-yr running means of PDO index (<http://research.jisao.washington.edu/pdo/>) and
234 AMO index from Trenberth and Shea (2006; <http://www.cgd.ucar.edu/cas/catalog/climind/AMO.html>) based on
235 HadISST (Rayner et al. 2003) for 1901–2010. Since the late 20th century, PDO and AMO tend to have opposite
236 signs. During the period with negative PDO and positive AMO (1951–1965 and 2003–2010), the wUS tends to
237 be warmer and dryer (Fig. 3d–f) compared with the period with positive PDO and negative AMO (1978–1999;
238 Fig. 3d–f). The recent global-warming hiatus (e.g. Delworth et al. 2015) is concurrent with a negative PDO and
239 positive AMO.

240 The Pacific and Atlantic SST variations influence the wUS climate on interannual-to-multidecadal
241 timescales (e.g. Seager et al. 2005; Meehl and Hu 2006; Cook et al. 2011; Dai 2013). Despite the dominant role
242 of ENSO in IAV in wintertime precipitation, the Atlantic Ocean contributes substantially to the summertime
243 precipitation (Feng et al. 2011). However, the AMO effect examined in AGCMs does not fully explain the total
244 precipitation variability over the wUS (Fig. 7 in Mo et al. 2009; Fig. 4 in Hu et al. 2011). Mo et al. (2009)
245 revealed that the direct influence of the Atlantic SST is limited but a combination of warm (cool) Atlantic and
246 cool (warm) Pacific results in amplified precipitation variability over the wUS. Hu and Feng (2012) suggested
247 that the Atlantic influence on the summertime precipitation over the tropical and subtropical North America is
248 sensitive to the Pacific SST anomaly. These studies suggested an importance of combination of PDO and AMO
249 on the wUS climate. In the next section, we try to decompose the DMV of historical climate over the wUS into

250 internal atmospheric variability and forced atmospheric response to SST variability over the Pacific and Atlantic
251 Oceans by using the large ensemble simulation.

252

253 **4. Global variability associated with the western-US climate on decadal-to-multidecadal timescale**

254 **4.1 SST, atmospheric circulation and precipitation**

255 In this section, we examine forced atmospheric response to the Pacific and Atlantic SST variability on
256 multidecadal timescale. Figure 4 shows DMV in precipitation and SST associated with negative PDO and
257 positive AMO. We detrended the variables for 1951–2010 before making a composite of “negative PDO and
258 positive AMO” periods (1951–1968 and 2003–2010) minus “positive PDO and negative AMO” period (1978–
259 1999). Substantial regionality in the precipitation anomaly including reduced precipitation over the mid-latitude
260 wUS (Figs. 3c, f, 4a) and East Asia (Ueda et al. 2015) is accompanied with negative tropical eastern Pacific and
261 positive North Atlantic SST anomalies (Fig. 4c). Meanwhile, increased precipitation is found over tropical
262 Central and South America (Fig. 4a). These precipitation anomalies can be found in the AGCM simulations with
263 statistical significance (Fig. 4b). The NW run also exhibits a similar precipitation pattern (Fig. S1 in the online
264 supplement). The interhemispheric SST gradient between the Northern (warm) and Southern (cool) Atlantic
265 associated with the AMO (Fig. 4c) intensifies summertime rainfall in the intertropical convergence zone (ITCZ)
266 over North Africa, Atlantic Ocean and Central and northern South America (Fig. 4a, b; Zhang and Delworth
267 2006; Mohino et al. 2011; Brönnimann et al. 2015).

268 Previous studies showed a dominant contribution of the tropical eastern Pacific SST to the wUS
269 precipitation variability (Seager et al. 2005; Meehl and Hu 2006; Dai 2013; Burgman and Jang 2015; Delworth
270 et al. 2015). Figure 5 shows a composite of “negative-PDO and negative-AMO” period (1966–1977) minus
271 “positive-PDO and positive-AMO” period (2000–2002). SST anomalies over the eastern tropical Pacific and the
272 Atlantic are similar and opposite to those in Fig. 4, respectively. Over the North Pacific, SST and precipitation
273 anomalies are quite different between the two (e.g. reduced and increased rainfall around the Hawaii Islands in
274 Figs. 4b and 5b, respectively), except the high SST anomaly over the mid-latitude eastern North Pacific (140°W;
275 35°N). The precipitation anomaly over North America (Fig. 5) is distinct from Fig. 4, suggesting that the Atlantic
276 SST is also important for the DMV in wUS precipitation in addition to the eastern Pacific SST.

277 DMV in tropical precipitation drives anomalous atmospheric circulation patterns from the tropics to
278 middle latitude (Kushnir et al. 2010; Trenberth et al. 2014; Ding et al. 2014). Figure 6 shows satellite-based
279 precipitation anomaly associated with DMV in SST over the Pacific and Atlantic Ocean since 1979 (2003–2010
280 minus 1979–1999). Note that the comparing period is slightly different from Fig. 4 because of limited data
281 availability. Rainfall anomalies over the tropical Pacific, Atlantic and wUS are overall consistent with land
282 observations and the AGCM simulations (Fig. 4a, b). Note that differences between the ensemble mean of the
283 AGCM simulations (Fig. 4b) and observations (Fig. 6; e.g. middle and high latitudes North Atlantic, North
284 Indian Ocean, western North Pacific, and middle latitude North Pacific) are not negligible. Figure 7 shows
285 atmospheric circulation anomalies associated with the negative PDO and positive AMO (1958–1968 and 2003–
286 2010 minus 1978–1998). Low-level cold and dry northerly and northwesterly anomaly over the wUS associated

287 with an intensified North Pacific anticyclone (positive geopotential height over the North Pacific; Fig. 7a) results
288 in a reduction of summertime precipitation over the wUS (Figs. 4a, 6; e.g. Dai 2013). In addition, the warm
289 tropical Atlantic (Fig. 4c) induces Gill-type atmospheric response (i.e. anomalous upper-level subtropical
290 anticyclones over Africa, Atlantic Ocean and America; Kamae et al. 2014a, and low-level cyclonic circulation
291 including easterly over Florida and westerly over south of Gulf of Mexico) and resultant reduction of moisture
292 advection from the Gulf of Mexico to Central North America (Fig. 7a; Kushnir et al. 2010; Feng et al. 2011; Hu
293 and Feng 2012). The observed anomalies above are consistent with those in the ensemble mean of the ALL run
294 (Fig. 7b) and the NW run (Fig. S2 in the online supplement), indicating a contribution of forced atmospheric
295 response to the natural DMV in SST (Fig. 4c). In addition, a mid-latitude wave-like pattern from the Pacific to
296 Atlantic (positive upper-level geopotential height anomaly over the North Pacific, south of Greenland, the
297 Canary Islands and negative anomaly over Canada and North Atlantic) can be found both in observations and the
298 forced atmospheric response in the AGCM run (Fig. 7a, b). Note that the forced atmospheric response to the SST
299 DMV obtained from the ensemble mean is generally smaller than that in the reanalysis, suggesting an important
300 role of atmospheric internal variability.

301

302 **4.2 Atmospheric response to tropical forcing**

303 During the period from the end of the 20th century to the early 21st century, the large DMV in the tropical
304 SST affects the mid-latitude climate by changing tropical convection and atmospheric circulations (Trenberth et
305 al. 2014; Ding et al. 2014; Ueda et al. 2015). To understand physical relationship between the DMV in tropical

306 precipitation (Figs. 4, 6) and the middle latitude atmospheric circulation (Fig. 7), idealized simulations were
307 performed by using LBM (Sect. 2.3). In Fig. 6, statistically-significant precipitation anomalies on multidecadal
308 timescale are found on the edge of ITCZ in the tropical eastern Pacific (ePac; centered at 140°W, 20°N) and over
309 the tropical Atlantic-to-African ITCZ (tAtl; centered at 5°W, 12°N; rectangles in Fig 6). It is worthwhile to note
310 that these precipitation anomalies cannot be found during the in-phase period of the PDO and AMO (Fig. 5).
311 Figure 8 shows profiles of climatological condensational heating over ePac and tAtl. Near-surface cooling
312 associated with the evaporation of cloud water is common to both regions while substantial heating is found in
313 the lower troposphere over ePac and in the middle troposphere over tAtl (e.g. Yanai and Tomita 1998; Shige et al.
314 2008; Hagos et al. 2010). Peak levels of anomalies associated with the DMV are similar to the climatologies
315 over ePac (not shown) and tAtl (Fig. 5b in Kushnir et al. 2010). To conduct LBM simulations, tropospheric
316 cooling and heating were made based on area-averaged precipitation anomalies in Fig. 6. The imposed heating
317 exhibits an oval shape with a spread of 40° (50°) longitude and 12° latitude over ePac (tAtl) with a heating
318 maximum at the center. Over ePac (tAtl), the cooling (heating) has a shallow (deep) vertical structure that peaks
319 at ~900 (450) hPa, where the maximum cooling (heating) rate is -0.43 (0.19) K day^{-1} . The response at day 20 is
320 analyzed when the model reaches a quasi-steady state.

321 Figure 9 shows quasi-steady atmospheric responses to the tropical heating/cooling. The diabatic cooling
322 due to the reduced condensation heat release over ePac (blue circle in Fig. 9a) induces a local low-level cyclonic
323 anomaly over the tropical Pacific and upper-level anticyclonic anomaly over the North Pacific. In the lower
324 troposphere, an anticyclonic circulation anomaly and northerly anomaly can be found over the North Pacific and

325 the wUS (Fig. 9a). The upper-level wave-like pattern from the mid-latitude Pacific to Atlantic (Fig. 9a) is similar
326 to observations and the ALL run (Fig. 7). The heating anomaly over tAtl results in upper-level subtropical
327 anticyclones and low-level cyclonic circulation over the Gulf of Mexico (easterly over Florida and westerly over
328 south of Gulf of Mexico; Fig. 9b; Kushnir et al. 2010; Feng et al. 2011), consistent with observations (Fig. 7).
329 These results indicate that the atmospheric responses to the two condensational heating can largely explain the
330 observed anomalies in the atmospheric circulation over the Pacific to Atlantic Oceans and associated wUS
331 precipitation (Figs. 4, 6, 7). Note that the simulated steady responses in the geopotential height and atmospheric
332 circulation are relatively weaker than observations and the ALL run. Contributions from other factors including
333 middle latitude SST anomalies may also be important for the DMV in atmospheric circulation and precipitation
334 (Ting and Wang 1997; Burgman and Jang 2015).

335

336 **5. Internal variability and forced atmospheric response**

337 As shown in the previous sections, the forced atmospheric responses to the SST DMV associated with
338 PDO and AMO over the wUS (Figs. 4b, 7b) are consistent with observations since the late 20th century (Figs. 4a,
339 6, 7a) when the PDO and AMO tend to be opposite in phase (Figs. 3–5). The idealized model simulation also
340 supports the tropical influence on the DMV in the mid-latitude atmospheric circulation (Fig. 9). These results
341 suggest that the forced atmospheric response to the SST DMV is important for the DMV in mid-latitude climate
342 despite internal atmospheric variability (e.g. Deser et al. 2012). In this section, we compared forced signal and

343 internal atmospheric variability using the ensemble simulations. Here a ratio R of forced response to internal
344 variability (signal-to-noise ratio; Mei et al. 2014, 2015) can be determined as:

$$345 \quad R = \frac{\sigma_F}{\sigma_I}, \quad (1)$$

346 where σ_F (forced response) is the standard deviation of the ensemble mean and σ_I (internal variability) is the
347 standard deviation of the departures from the ensemble mean in the 100 members. Before the calculation,
348 long-term trends (for 1951–2010) were removed from variables. A large R indicates a relatively important role of
349 forced response compared with internal variability and thus a high potential predictability. We examine R on two
350 different timescales: interannual (shorter than 15 years) and multidecadal (longer than or equal to 15 years). To
351 examine R on multidecadal timescales, 15-yr running mean of given variables were used for calculating σ_F and σ_I .
352 Residuals obtained by removing the running mean were used for calculation R on interannual timescale. We also
353 tested results by using other criteria (e.g. 11 years) and confirmed that spatial patterns and relative importance
354 (detailed below) were not sensitive to selection of criteria.

355 Figure 10 compares R during JJA for 1951–2010 on the two timescales. In general, contribution of
356 atmospheric internal variability to the mid-latitude high-frequency (shorter than 15 years) variability is dominant
357 (Fig. 10a, c; e.g. Madden 1976). In the middle latitudes, R is larger (i.e. the relative contribution of SST-forced
358 response becomes more dominant) for low-frequency (longer than or equal to 15 years) variability (Fig. 10b, d)
359 than for the high-frequency variability (Fig. 10a, c). R is also larger over the tropics and Greenland on the longer
360 timescale. Although large R values in precipitation on both timescales are generally confined to the tropics (Fig.
361 10c, d), they can also be found over the mid-latitude wUS, North Africa, northern India and southeastern China.

362 These results suggest a potential higher predictability of the SAT and precipitation on multidecadal than
363 interannual timescale. Figure 11 shows R during December, January and February. The dominant role of
364 middle-latitude atmospheric internal variability during boreal winter (e.g. Deser et al. 2012) results in a smaller R
365 than JJA. For mid-latitude SAT, R is also larger on multidecadal than interannual timescale (Fig. 11a, b),
366 although R for wintertime precipitation is not substantially different between the two timescales (Fig. 11c, d). We
367 also confirmed that results of the NW run (Figs. S3 and S4 in the online supplement) are generally similar to
368 Figs. 10 and 11 because long-term trend were removed before calculating R and IAV and DMV are similar
369 between the two runs.

370 The prolonged periods with oppositely phased PDO and AMO since the late 20th century result in the
371 substantial forced atmospheric response to the SST variability over the wUS during boreal summer on the
372 multidecadal timescale. In contrast to winter, relatively weaker influence of atmospheric internal variability (e.g.
373 Deser et al. 2012) results in the larger R during the summer, suggesting a potential predictability of summertime
374 climate on the multidecadal timescale. Note that the DMV in summertime wUS climate is substantially weaker
375 during the periods when PDO and AMO are in phase (Fig. 5), suggesting that the wUS R could be sensitive to
376 relative phase between the two modes.

377

378 **6. Summary and discussion**

379 By comparing observations and the large member ensemble AGCM simulations, we have evaluated the
380 SST-forced atmospheric response in the middle latitudes for the recent 60 years. The anthropogenically-induced

381 climate trends contributed to the long-term increase in mean temperature and frequency of hot summers over the
382 wUS and the Northern Hemisphere land areas. On the decadal-to-multidecadal timescale, the remarkable
383 SST-forced signal is identified in the wUS summertime climate. PDO and AMO tend to be in opposite phase
384 since the late 20th century, resulting in the amplified DMV in the wUS climate. During the negative PDO and
385 positive AMO periods, low-level northerly wind anomaly over the wUS and cyclonic circulation anomaly over
386 the subtropical North Atlantic result in reduced moisture advection and summertime precipitation over central
387 and western North America. The wave-like atmospheric circulation pattern associated with the DMV can largely
388 be reproduced by the AGCM runs and the idealized atmospheric simulations, indicating the importance of
389 atmospheric teleconnections initiated by the tropical diabatic heating associated with the negative PDO and
390 positive AMO. The recent wUS climate anomaly since the early 21st century (persistent warm and dry condition)
391 can partly be attributed to the DMV modes over the Pacific and Atlantic. The robust forced component of wUS
392 summertime climate anomalies suggests a potential predictability on multidecadal timescale.

393 In this study, we only focused on the atmospheric variables including air temperature, precipitation and
394 atmospheric circulation. SAT variation over land is also tightly associated with the regional hydrological cycle
395 (runoff, precipitation minus evaporation, and soil moisture content; Seneviratne et al. 2010; Langford et al. 2014;
396 Chikamoto et al. 2015; Yoon and Leung 2015). Variation in soil moisture (including drought) influences on the
397 surface energy balance and resultant variations in frequency of extreme climate events including heat waves
398 (Mueller and Seneviratne 2012). The effect of land hydrological cycle and underlying physical mechanisms
399 should be examined in future studies.

400 This study demonstrated the utility of the 100-member ensemble in isolating the forced atmospheric
401 response (i.e. high statistical significance despite the substantial internal atmospheric variability in the middle
402 latitudes; e.g. Mori et al. 2014). The good reproducibility of the global climate variations highlights the potential
403 for probabilistic attribution studies. We only examined monthly-mean data, but extreme climate phenomena on
404 the sub-daily, daily, and weekly timescales should be further examined (i.e. tropical cyclones, atmospheric
405 blocking, severe storms and resultant temperature, wind and precipitation extremes). In addition, the high
406 resolution model is suitable for examining variations in regional atmospheric circulation and rainfall patterns
407 induced by orography (Xie et al. 2006; Endo et al. 2012; Kusunoki and Arakawa 2012; Langford et al. 2014;
408 Nakaegawa et al. 2014). The use of this ensemble dataset also aids risk assessments via statistical analyses of the
409 high-impact climate events.

410

411 **Acknowledgements**

412 The authors thank anonymous reviewers for giving us constructive comments. This work was supported by
413 the Program for Risk Information on Climate Change (SOUSEI program) and the Data Integration and Analysis
414 System (DIAS) sponsored by the Ministry of Education, Culture, Sports, Science and Technology (MEXT),
415 Japan. The Earth Simulator was used to develop the d4PDF ensemble dataset as “Strategic Project with Special
416 Support” of JAMSTEC. The d4PDF dataset is available via DIAS website
417 (http://dias-dss.tkl.iis.u-tokyo.ac.jp/ddc/viewer?ds=d4PDF_GCM&lang=en).

418

419 **References**

- 420 Adler RF, Huffman GJ, Chang A et al (2003) The Version-2 Global Precipitation Climatology Project (GPCP)
421 monthly precipitation analysis (1979-present). *J Hydrometeorol* 4:1147–1167
- 422 Brewer M, Mass C (2016) Projected changes in heat extremes and associated synoptic/mesoscale conditions over
423 the northwest U.S. *J Clim*. doi:10.1175/JCLI-D-15-0641.1
- 424 Brönnimann S, Fischer AM, Rozanov E, Poli P, Compo GP, Sardeshmukh PD (2015) Southward shift of the
425 northern tropical belt from 1945 to 1980. *Nature Geosci* 8:969–974
- 426 Burgman RJ, Jang Y (2015) Simulated U.S. drought response to interannual and decadal Pacific SST variability.
427 *J Clim* 28:4688–4705
- 428 Chikamoto Y, Timmermann A, Stevenson S, DiNezio P, Langford S (2015) Decadal predictability of soil water,
429 vegetation, and wildfire frequency over North America. *Clim Dyn* 45:2213–2235
- 430 Christidis N, Stott PA (2014) Change in the odds of warm years and seasons due to anthropogenic influence on
431 the climate. *J Clim* 27:2607–2621
- 432 Cook ER, Seager R, Cane MA, Stahle DW (2007) North American drought: reconstructions, causes and
433 consequences. *Earth Sci Rev* 81:93–134
- 434 Cook BI, Cook ER, Anchukaitis KJ, Seager R, Miller RL (2011) Forced and unforced variability of twentieth
435 century North American droughts and pluvials. *Clim Dyn* 37:1097–1110
- 436 Dai A (2013) The influence of the inter-decadal Pacific oscillation on US precipitation during 1923–2010. *Clim*
437 *Dyn* 41:633–646

438 Delworth TL, Zeng F, Rosati A, Vecchi G, Wittenberg A (2015) A link between the hiatus in global warming and
439 North American drought. *J Clim* 28:3834–3845

440 Deser C, Phillips AS, Hurrell JW (2004) Pacific interdecadal climate variability: linkages between the tropics
441 and the North Pacific during boreal winter since 1900. *J Clim* 17:3109–3124

442 Deser C, Knutti R, Solomon S, Phillips AS (2012) Communication of the role of natural variability in future
443 North American climate. *Nature Clim Change* 2:775–779

444 Diffenbaugh NS, Swain DL, Touma D (2015) Anthropogenic warming has increased drought risk in California.
445 *Proc Natl Acad Sci USA* 112:3931–3936

446 Ding Q, Wallace JM, Battisti DS, Steig EJ, Gallant AJE, Kim H.-J, Geng L (2014) Tropical forcing of the recent
447 rapid Arctic warming in northeastern Canada and Greenland. *Nature* 509:209–212

448 Endo H, Kitoh A, Ose T, Mizuta R, Kusunoki S (2012) Future changes and uncertainties in Asian precipitation
449 simulated by multiphysics and multi-sea surface temperature ensemble experiments with high-resolution
450 Meteorological Research Institute atmospheric general circulation models (MRI-AGCMs). *J Geophys Res*
451 117:D16118. doi:10.1029/2012JD017874

452 England MH et al (2014) Recent intensification of wind-driven circulation in the Pacific and the ongoing
453 warming hiatus. *Nature Clim Change* 4:222–227

454 Eyring V et al (2005) A strategy for process-oriented validation of coupled chemistry-climate models. *Bull Am*
455 *Meteorol Soc* 86:1117–1133

456 Feng S, Hu Q, Oglesby RJ (2011) Influence of Atlantic sea surface temperatures on persistent drought in North
457 America. *Clim Dyn* 37:569–586. doi:10.1007/s00382-010-0835-x

458 Fyfe JC et al (2016) Making sense of the early-2000s warming slowdown. *Nature Clim Change* 6:224–228

459 Gu F, Adler RF, Huffman GJ (2016) Long-term changes/trends in surface temperature and precipitation during
460 the satellite era (1979–2012). *Clim Dyn* 46:1091–1105

461 Hansen J, Sato M, and Ruedy R (2012) Perception of climate change. *Proc Natl Acad Sci USA* 109:E2415–
462 E2423

463 Harris I, Jones PD, Osborn TJ, Lister DH (2014) Updated high-resolution grids of monthly climatic observations
464 – the CRU TS3.10 Dataset. *Int J Climatol* 34:623–642

465 Hagos S et al (2010) Estimates of tropical diabatic heating profiles: Commonalities and uncertainties. *J Clim*
466 23:542–558

467 Hawkins E, Sutton R (2009) The potential to narrow uncertainty in regional climate predictions. *Bull Am*
468 *Meteorol Soc* 90:1095–1107

469 Hirahara S, Ishii M, Fukuda Y (2014) Centennial-scale sea surface temperature analysis and its uncertainty. *J*
470 *Clim* 27:57–75

471 Hoerling M, Eischeid J, Perlwitz J (2010) Regional precipitation trends: distinguishing natural variability from
472 anthropogenic forcing. *J Climate* 23:2131–2145

- 473 Hu Q, Feng S (2012) AMO- and ENSO-driven summertime circulation and precipitation variations in North
474 America. *J Clim* 25:6477–6495
- 475 Hu Q, Feng S, Oglesby RJ (2011) Variations in North American summer precipitation driven by the Atlantic
476 Multidecadal Oscillation. *J Clim* 24:5555–5570
- 477 IPCC (2013) Summary for policymakers, in *Climate Change 2013: The Physical Science Basis*, edited by
478 Stocker TF et al, pp. 3–29, Cambridge Univ Press, Cambridge, UK, and New York.
479 doi:10.1017/cbo9781107415324.004
- 480 Jones GS, Stott PA, Christidis N (2013) Attribution of observed historical near surface temperature variations to
481 anthropogenic and natural causes using CMIP5 simulations. *J Geophys Res Atmos* 118:4001–4024.
482 doi:10.1002/jgrd.50239
- 483 Kamae Y, Shiogama H, Watanabe M, Kimoto M (2014a) Attributing the increase in Northern Hemisphere hot
484 summers since the late 20th century. *Geophys Res Lett* 41:5192–5199
- 485 Kamae Y, Watanabe M, Kimoto M, Shiogama H (2014b) Summertime land–sea thermal contrast and
486 atmospheric circulation over East Asia in a warming climate—Part I: Past changes and future projections.
487 *Clim Dyn* 43:2553–2568
- 488 Kamae Y, Shiogama H, Watanabe M, Ishii M, Ueda H, Kimoto M (2015) Recent slowdown of tropical upper
489 tropospheric warming associated with Pacific climate variability. *Geophys Res Lett* 42: 2995–3003

490 Kobayashi S et al (2015) The JRA-55 Reanalysis: General specifications and basic characteristics. *J Meteorol*
491 *Soc Jpn* 93:5–48

492 Kosaka Y, Xie S-P (2013) Recent global-warming hiatus tied to equatorial Pacific surface cooling. *Nature*
493 501:403–407

494 Kushnir Y, Seager R, Ting MF, Naik N, Nakamura J (2010) Mechanisms of tropical Atlantic SST influence on
495 North American precipitation variability. *J Clim* 23:5610–5628

496 Kusunoki S, Arakawa O (2012) Change in the precipitation intensity of the East Asian summer monsoon
497 projected by CMIP3 models. *Clim Dyn* 38:2055–2072

498 Langford S, Stevenson S, Noone D (2014) Analysis of low-frequency precipitation variability in CMIP5
499 historical simulations for southwestern North America. *J Clim* 27:2735–2756

500 Li X, Xie S-P, Gille ST, Yoo C (2016) Atlantic-induced pan-tropical climate change over the past three decades.
501 *Nature Clim Change* 6:275–279

502 Luo JJ, Sasaki W, Masumoto Y (2012) Indian Ocean warming modulates Pacific climate change. *Proc Natl Acad*
503 *Sci USA* 109:18701–18706

504 Madden RA (1976) Estimates of the natural variability of time-averaged sea-level pressure. *Mon Wea Rev*
505 104:942–952

506 Mantua NJ, Hare SR, Zhang Y, Wallace JM, Francis RC (1997) A Pacific interdecadal climate oscillation with
507 impacts on salmon production. *Bull Am Meteorol Soc* 78:1069–1079

508 McGregor S et al (2014) Recent Walker circulation strengthening and Pacific cooling amplified by Atlantic
509 warming. *Nature Clim Change* 4:888–892

510 Meehl GA, Hu AX (2006) Megadroughts in the Indian monsoon region and southwest North America and a
511 mechanism for associated multidecadal Pacific sea surface temperature anomalies. *J Clim* 19:1605–1623

512 Meehl GA, Arblaster JM, Tebaldi C (2007) Contributions of natural and anthropogenic forcing to changes in
513 temperature extremes over the U.S. *Geophys Res Lett* 34:L19709. doi:10.1029/2007GL030948

514 Meehl GA, Arblaster JM, Branstator G (2012) Mechanisms contributing to the warming hole and the consequent
515 U.S. east–west differential of heat extremes. *J Clim* 25:6394–6408

516 Mei W, Xie S-P, Zhao M (2014) Variability of tropical cyclone track density in the North Atlantic: Observations
517 and high-resolution simulations. *J Clim* 27:4797–4814

518 Mei W, Xie S-P, Zhao M, Wang Y (2015) Forced and internal variability of tropical cyclone track density in the
519 western North Pacific. *J Clim* 28:143–167

520 Mizuta R, Yoshimura H, Murakami H, Matsueda M, Endo H, Ose T, Kamiguchi K, Hosaka M, Sugi M,
521 Yukimoto S, Kusunoki S, Kitoh A (2012) Climate simulations using MRI-AGCM with 20-km grid. *J*
522 *Meteorol Soc Jpn* 90A:235–260

523 Mizuta R et al (2016) Over 5000 years of ensemble future climate simulations by 60km global and 20km
524 regional atmospheric models. *Bull Am Meteorol Soc* (submitted)

525 Mo K, Schemm J, Yoo S (2009) Influence of ENSO and the Atlantic Multidecadal Oscillation on drought over
526 the United States. *J Clim* 22:5962–5982

527 Mohino E, Janicot S, Bader J (2011) Sahel rainfall and decadal to multi-decadal sea surface temperature
528 variability. *Clim Dyn* 37:419–440

529 Mori M, Watanabe M, Shiogama H, Inoue J, Kimoto M (2014) Robust Arctic sea-ice influence on the frequent
530 Eurasian cold winters in past decades. *Nat Geosci* 7:869–873

531 Mueller B, Seneviratne SL (2012) Hot days induced by precipitation deficits at the global scale. *Proc Natl Acad
532 Sci USA* 109:12398–12403

533 Murakami H, Mizuta R, Shindo E (2012) Future changes in tropical cyclone activity projected by multi-physics
534 and multi-SST ensemble experiments using the 60-km-mesh MRI-AGCM. *Clim Dyn* 39:2569–2584

535 Nakaegawa T, Kitoh A, Murakami H, Kusunoki S (2014) Annual maximum 5-day rainfall total and maximum
536 number of consecutive dry days over Central America and the Caribbean in the late twenty-first century
537 projected by an atmospheric general circulation model with three different horizontal resolutions. *Theor
538 Appl Climatol* 116:155–168

539 Newman M. et al (2016) The Pacific Decadal Oscillation, revisited. *J Clim* 29:4399–4427

540 Perkins SE, Alexander LV, Nairn JR (2012) Increasing frequency, intensity and duration of observed global
541 heatwaves and warm spells. *Geophys Res Lett* 39:L20714. doi:10.1029/2012GL053361

542 Prein AF, Holland GJ, Rasmussen RM, Clark MP, Tye MR (2016) Running dry: The U.S. Southwest's drift into a
543 drier climate state. *Geophys Res Lett* 43:1272–1279

544 Power S, Casey T, Folland C, Colman A, Mehta V (1999) Interdecadal modulation of the impact of ENSO on
545 Australia. *Clim Dyn* 15:319–324

546 Rayner NA et al (2003) Global analyses of sea surface temperature, sea ice, and night marine air temperature
547 since the late nineteenth century. *J Geophys Res* 108(D14):4407. doi:10.1029/2002JD002670

548 Seager R, Hoerling M (2014) Atmosphere and ocean origins of North American droughts. *J Clim* 27:4581–4606

549 Seager R, Kushnir Y, Herweijer C, Naik N, Velez J (2005) Modeling of tropical forcing of persistent droughts
550 and pluvials over western North America: 1856–2000. *J Clim* 18:4068–4091

551 Seneviratne SI, Corti T, Davin EL, Hirschi M, Jaeger EB, Lehner I, Orlowsky B, Teuling AJ (2010) Investigating
552 soilmoisture-climate interactions in a changing climate: A review. *Earth Sci Rev* 99:125–161

553 Sheffield J et al (2013) North American climate in CMIP5 experiments. Part II: Evaluation of historical
554 simulations of intraseasonal to decadal variability. *J Clim* 26:9247–9290

555 Shibata K, Deushi M, Sekiyama TT, Yoshimura H (2005) Development of an MRI chemical transport model for
556 the study of stratospheric chemistry. *Pap Meteor Geophys* 55:75–118

557 Shige S, Takayabu YN, Tao W-K (2008) Spectral retrieval of latent heating profiles from TRMM PR data. Part
558 III: Estimating apparent moisture sink profiles over tropical oceans. *J Appl Meteorol Climatol* 47:620–640

559 Shiogama H, Watanabe M, Imada Y, Mori M, Kamae Y, Ishii M, Kimoto M (2014) Attribution of the June-July
560 2013 heat wave in the southwestern United States. SOLA 10:122–126

561 Shiogama H et al (2016) Attributing historical changes in probabilities of record-breaking daily temperature and
562 precipitation extreme events. SOLA 12:225–231

563 Sippel S, Zscheischler J, Heimann M, Otto FEL, Peters J, Mahecha MD (2015) Quantifying changes in climate
564 variability and extremes: Pitfalls and their overcoming. Geophys Res Lett 42:9990–9998

565 Sutton RT, Hodson DLR (2005) Atlantic Ocean forcing of North American and European summer climate.
566 Science 309:115–118

567 Sutton RT, Hodson DLR (2007) Climate response to basin-scale warming and cooling for the North Atlantic
568 Ocean. J Clim 20:891–907

569 Ting M, Wang H (1997) Summertime US precipitation variability and its relation to Pacific sea surface
570 temperature. J Clim 10: 1853–1873

571 Trenberth KE, Shea DJ (2006) Atlantic hurricanes and natural variability in 2005. Geophys Res Lett 33:L12704.
572 doi:10.1029/2006GL026894

573 Trenberth KE, Fasullo JT, Branstator G, Phillips S (2014) Seasonal aspects of the recent pause in surface
574 warming. Nature Clim Change 4:911–916

575 Ueda H, Kamae Y, Hayasaki M, Kitoh A, Watanabe A, Miki Y, Kumai A (2015) Combined effects of recent
576 Pacific cooling and Indian Ocean warming on the Asian monsoon. Nature Comm 6:8854

577 Wallace JM, Deser C, Smoliak BV, Phillips AS (2015) Attribution of climate change in the presence of internal
578 variability. in *Climate Change: Multidecadal and Beyond*, World Scientific Series on Asia-Pacific Weather
579 and Climate Vol. 6, edited by Chang CP, Ghil M, Latif M, Wallace JM, pp. 1–29, World Scientific
580 Publishing

581 Wang B, Liu J, Kim HJ, Webster PJ, Yim SY, Xiang B (2013) Northern Hemisphere summer monsoon
582 intensified by mega-El Nino/southern oscillation and Atlantic multidecadal oscillation. *Proc Natl Acad Sci*
583 USA 110:5347–5352

584 Wang H, Schubert S (2014) The precipitation response over the continental United States to cold tropical Pacific
585 sea surface temperatures. *J Clim* 27:5036–5055

586 Watanabe M, Kimoto M (2000) Atmosphere–ocean thermal coupling in the North Atlantic: a positive feedback.
587 *Q J Roy Meteorol Soc* 126:3343–3369

588 Watanabe M, Shiogama H, Tatebe H, Hayashi M, Ishii M, Kimoto M (2014) Contribution of natural decadal
589 variability to global-warming acceleration and hiatus. *Nature Clim Change* 4:893–897

590 Xie S-P, Xu H, Saji NH, Wang Y, Liu WT (2006) Role of narrow mountains in large-scale organization of Asian
591 monsoon convection. *J Clim* 19:3420–3429

592 Xie S-P et al (2015) Towards predictive understanding of regional climate change. *Nature Clim Change* 5:921–
593 930

594 Yanai M, Tomita T (1998) Seasonal and interannual variability of atmospheric heat sources and moisture sinks as
595 determined from NCEP–NCAR reanalysis. *J Clim* 11:463–482

596 Yoon J-H, Leung LR (2015) Assessing the relative influence of surface soil moisture and ENSO SST on
597 precipitation predictability over the contiguous United States. *Geophys Res Lett* 42:5005–5013

598 Yukimoto S et al. (2011) Meteorological Research Institute-Earth System Model v1 (MRI-ESM1)—model
599 description. *Tech Rep Meteor Res Inst* 64, p 88 [available at
600 http://www.mri-jma.go.jp/Publish/Technical/DATA/VOL_64/index_en.html]

601 Zhang X, Hegerl G, Zwiers F, Kenyon J (2005) Avoiding inhomogeneity in percentile-based indices of
602 temperature extremes. *J Clim* 18:1641–1651

603 Zhang R, Delworth TL (2006) Impact of Atlantic multidecadal oscillations on India/Sahel rainfall and Atlantic
604 hurricanes. *Geophys Res Lett* 33:L17712. doi:10.1029/2006GL026267

605 Zhou Y, Wu Z (2016) Possible impacts of mega-El Niño/Southern Oscillation and Atlantic multidecadal
606 oscillation on Eurasian heat wave frequency variability. *Q J Roy Meteorol Soc* 142:1647–1661

607

608

609 **Table captions**

610

611 **Table 1.** Anomalies over the western US during 2000–2010 relative to 1978–1999. ALL and NW lines represent

612 results of 100-member AGCM simulations and non-warming simulations, respectively. ANT line is

613 anthropogenic influence, determined by ALL minus NW (Sect. 2.2). Uncertainty ranges represent 95%

614 confidence intervals

615

616 **Figure captions**

617

618 **Fig. 1** (a) Surface air temperature (SAT; K) anomalies averaged over the Northern Hemisphere land areas during
619 June-July-August (JJA) relative to 1958–1990 mean. Black and gray lines represent JRA-55 (1958–2010)
620 and CRU TS v3.23 (1901–2010), respectively. Red and blue lines and shadings are ensemble mean and 95%
621 confidence interval of 100-member ALL and NW runs (1951–2010), respectively. (b) Similar to (a) but for
622 anomalies (relative to 1958–1990) of areal fraction of hot summers (%) determined by mean and two
623 standard deviation of SAT during 1958–2010 (see section 2.4)

624

625 **Fig. 2** (a) JJA-mean SAT anomaly (K) during 2000–2010 relative to 1978–1999 in JRA-55. Stipples indicate
626 regions with statistically significant anomaly at 95% confidence level. Black rectangle represents the
627 western US region used in this study. (b) Similar to (a) but for ALL run. (c, d) Similar to (a, b) but for
628 frequency of hot summers (%)

629

630 **Fig. 3** (a, b) Similar to Fig. 1a, b but for SAT and frequency of hot summers averaged over the western US
631 (black rectangle in Fig. 2). (c) Precipitation anomalies (mm day^{-1}) over the western US. (d–f) Similar to (a–
632 c) but for 11-year running mean. (g) Anomalies of 11-year running mean indices of Pacific Decadal
633 Oscillation (PDO) and Atlantic Multidecadal Oscillation (AMO). Both of the indices are standardized for
634 1901–2010 period

635

636 **Fig. 4** Composite anomalies of JJA-mean precipitation and sea surface temperature (SST) for “negative PDO
637 and positive AMO” period (1951–1965 and 2003–2010) minus “positive PDO and negative AMO” period
638 (1978–1999). (a) Land precipitation (mm day^{-1}) in CRU TS v3.23. (b) Ensemble mean of ALL run. Only
639 statistically significant anomalies at 95% confidence level are shown. (c) SST (K) in HadISST

640

641 **Fig. 5** Similar to Fig. 4, but for “negative PDO and negative AMO” period (1966–1977) minus “positive PDO
642 and positive AMO” period (2000–2002)

643

644 **Fig. 6** JJA-mean precipitation anomaly (mm day^{-1}) in GPCP during 2003–2010 relative to 1979–1999. Stipples
645 indicate regions with statistically significant anomaly at 95% confidence level. Blue and red rectangles are
646 the eastern tropical Pacific (ePac) and tropical Atlantic (tAtl) regions used in Fig. 8, respectively

647

648 **Fig. 7** (a) Composite anomalies of JJA-mean atmospheric circulation for “negative PDO and positive AMO”
649 period (1958–1965 and 2003–2010) minus “positive PDO and negative AMO” period (1978–1999) in
650 JRA-55. Shading represents eddy component (anomaly from zonal mean) of geopotential height (m) at 200
651 hPa level. Vectors and contours are wind (m s^{-1}) and geopotential height ($\pm 1, 3, 10$ m) at 850 hPa level,

652 respectively. Solid and dashed contours represent positive and negative anomalies. (b) Similar to (a) but for
653 the ALL run. Only anomalies with 95% confidence level are shown

654

655 **Fig. 8** Climatological (1951–2010) atmospheric heating rate (K day^{-1}) due to large-scale condensation and
656 convective precipitation in JRA-55. Black solid and gray dashed lines are averages over the ePac and tAtl
657 regions shown in Fig. 6

658

659 **Fig. 9** Similar to Fig. 7, but for atmospheric response to tropical diabatic heating simulated in Linear Baroclinic
660 Model (Sect. 2.3). (a) Atmospheric response to lower-tropospheric cooling over ePac region centered at
661 140°W , 20°N (blue circle). Contours are geopotential height at 850 hPa level ($\pm 0.1, 0.5, 1$ m). (b) Similar to
662 (a) but for middle-tropospheric heating over tAtl region centered at 5°W , 12°N (red circle)

663

664 **Fig. 10** Signal-to-noise ratio during JJA determined by a ratio of standard deviation in 100-member ensemble
665 mean to standard deviation among the members. (a) High-frequency and (b) low-frequency SAT variation
666 shorter than 15 years and longer than or equal to 15 years, respectively. White contour represents 1.0. (c, d)
667 Similar to (a, b) but for precipitation

668

669 **Fig. 11** Similar to Fig. 10, but for December-January-February (DJF)

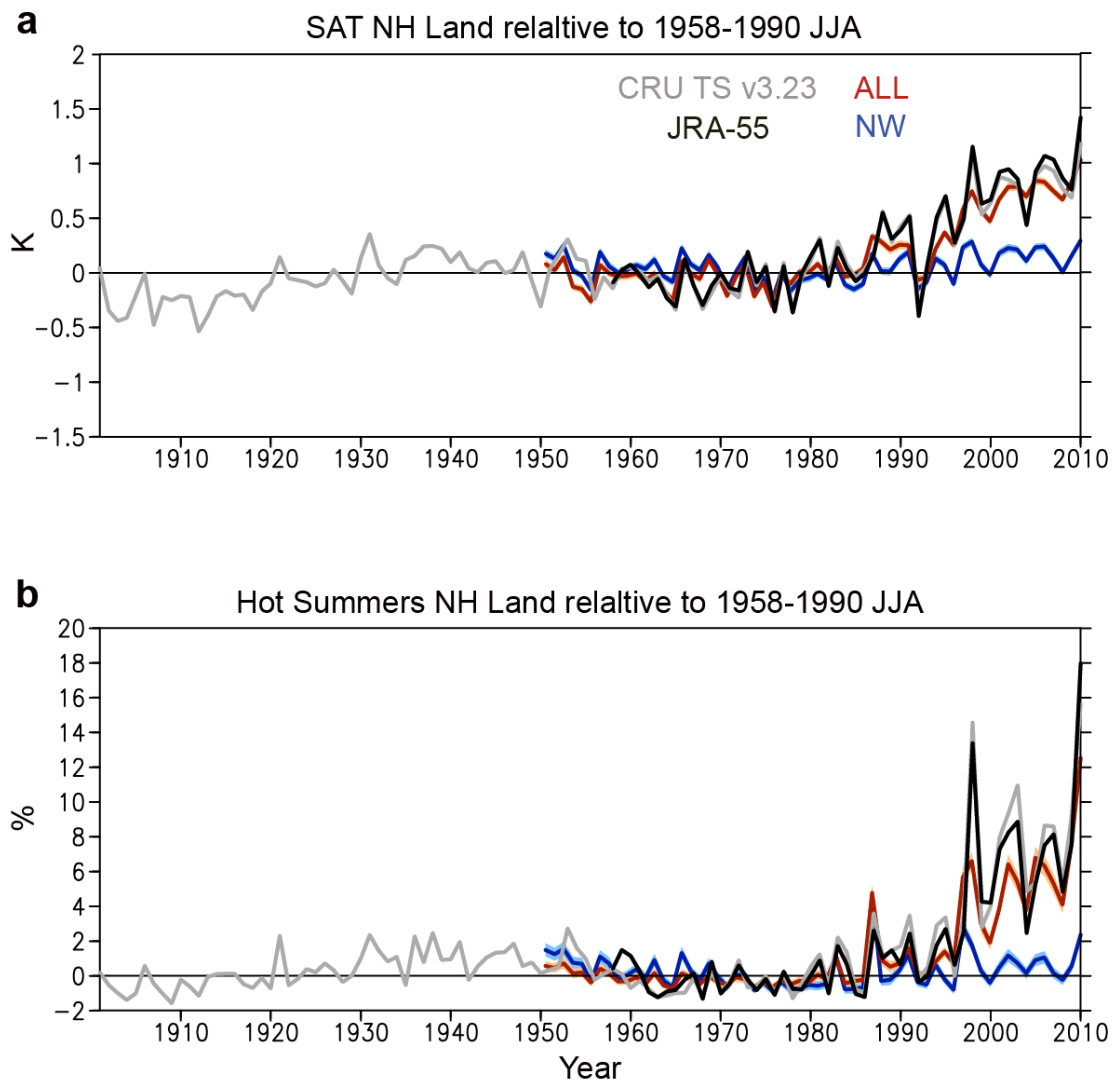
670 **Table 1.** Anomalies over the western US during 2000–2010 relative to 1978–1999. ALL and NW lines represent
671 results of 100-member AGCM simulations and non-warming simulations, respectively. ANT line is
672 anthropogenic influence, determined by ALL minus NW (Sect. 2.2). Uncertainty ranges represent 95%
673 confidence intervals

674

	SAT (K)	Hot summers (%)	Precipitation (mm day ⁻¹)
CRU TS v3.23	0.61 ± 0.57	2.64 ± 3.93	-0.14 ± 0.15
JRA-55	0.79 ± 0.69	4.20 ± 4.58	
ALL	0.74 ± 0.06	4.14 ± 0.53	-0.09 ± 0.02
NW	0.25 ± 0.06	0.76 ± 0.42	-0.04 ± 0.02
ANT	0.49 ± 0.08	3.38 ± 0.61	-0.05 ± 0.03

675

676



677

678

679 **Fig. 1** (a) Surface air temperature (SAT; K) anomalies averaged over the Northern Hemisphere land areas during

680 June-July-August (JJA) relative to 1958–1990 mean. Black and gray lines represent JRA-55 (1958–2010)

681 and CRU TS v3.23 (1901–2010), respectively. Red and blue lines and shadings are ensemble mean and

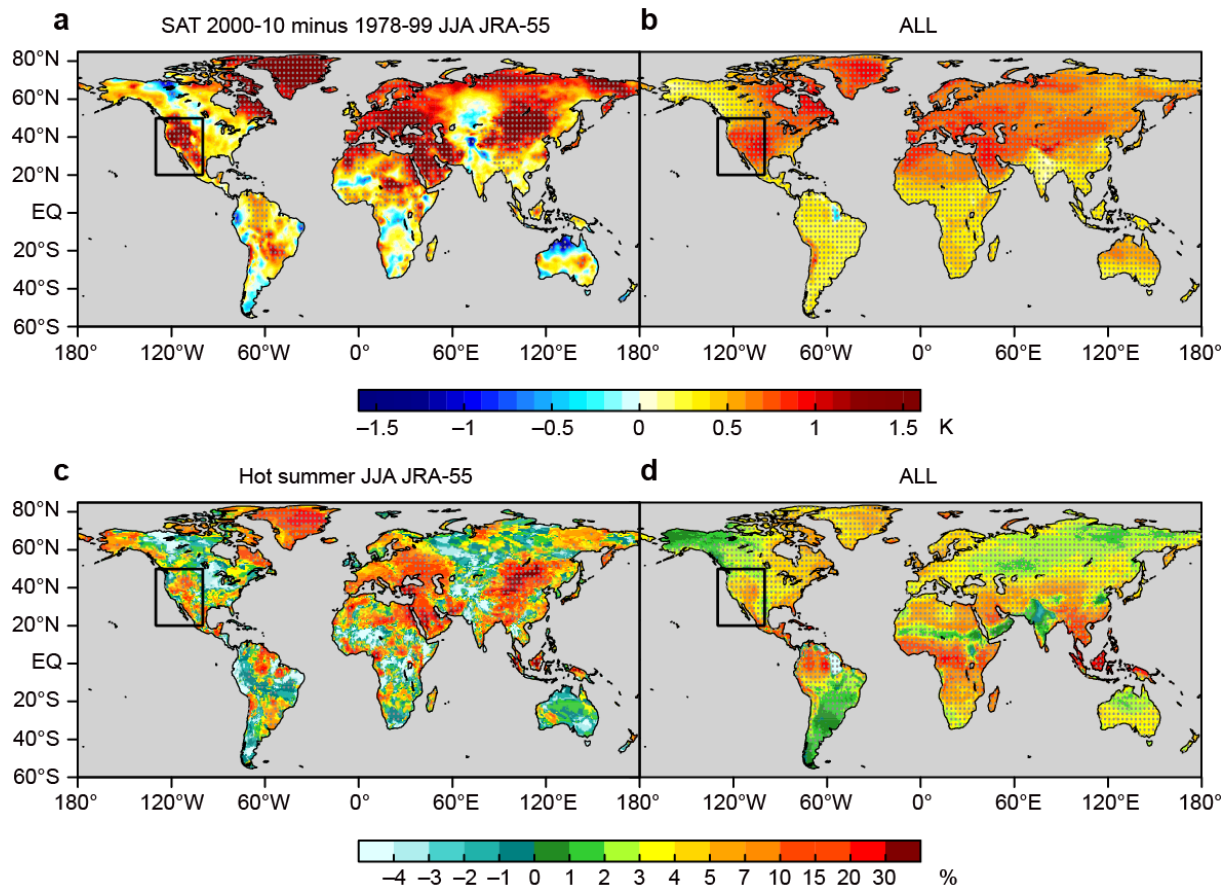
682 95% confidence interval of 100-member ALL and NW runs (1951–2010), respectively. (b) Similar to (a)

683 but for anomalies (relative to 1958–1990) of areal fraction of hot summers (%) determined by mean and

684 two standard deviation of SAT during 1958–2010 (see section 2.4)

685

686



687

688 **Fig. 2** (a) JJA-mean SAT anomaly (K) during 2000–2010 relative to 1978–1999 in JRA-55. Stipples indicate

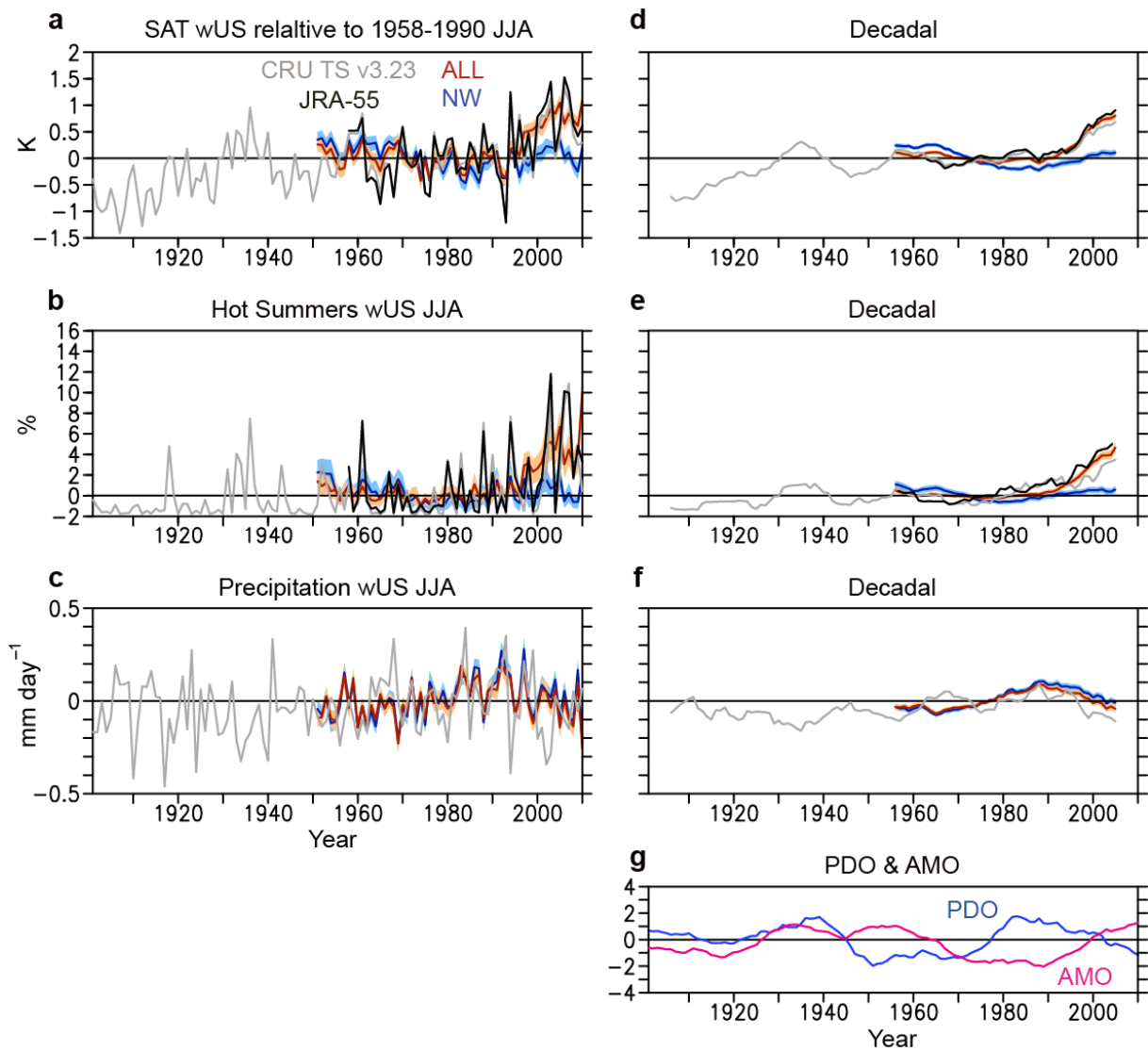
689 regions with statistically significant anomaly at 95% confidence level. Black rectangle represents the

690 western US region used in this study. (b) Similar to (a) but for ALL run. (c, d) Similar to (a, b) but for

691 frequency of hot summers (%)

692

693



694

695

696 **Fig. 3** (a, b) Similar to Fig. 1a, b but for SAT and frequency of hot summers averaged over the western US

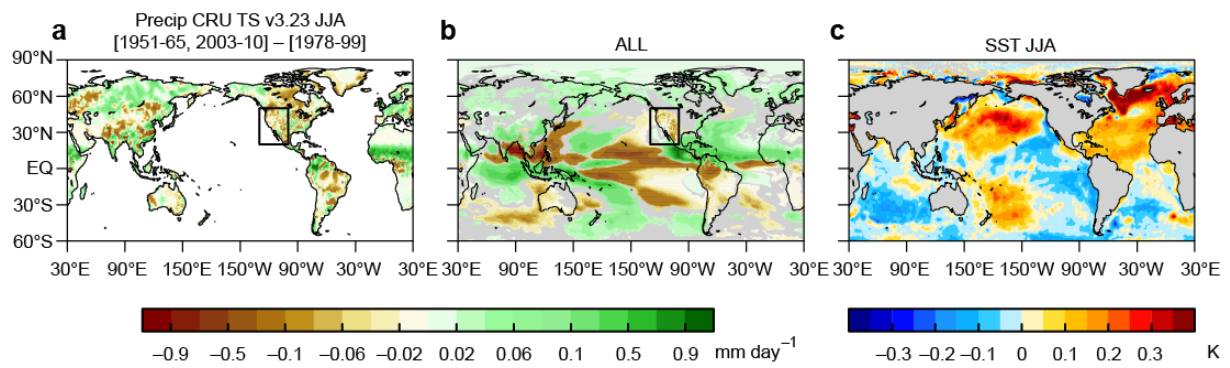
697 (black rectangle in Fig. 2). (c) Precipitation anomalies (mm day^{-1}) over the western US. (d–f) Similar to (a–

698 c) but for 11-year running mean. (g) Anomalies of 11-year running mean indices of the Pacific Decadal

699 Oscillation (PDO) and Atlantic Multidecadal Oscillation (AMO). Both of the indices are standardized for

700 1901–2010 period

701



702

703

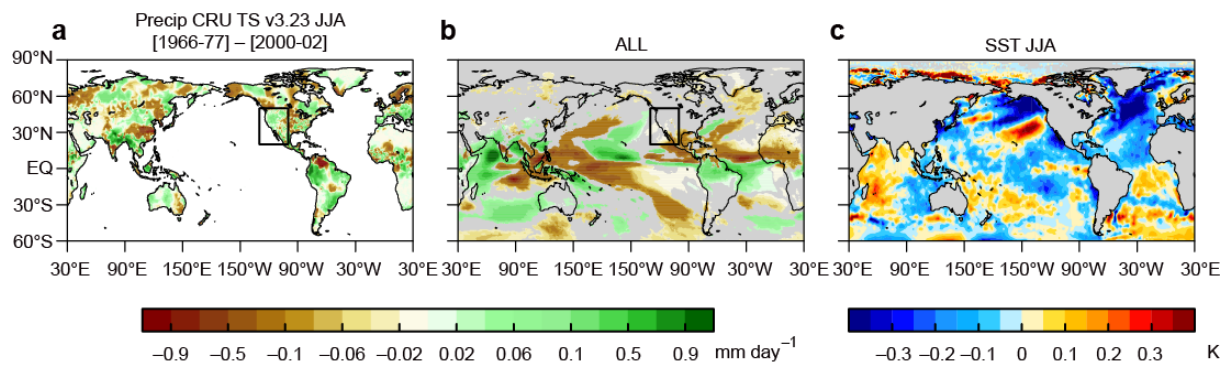
704 **Fig. 4** Composite anomalies of JJA-mean precipitation and sea surface temperature (SST) for “negative PDO

705 and positive AMO” period (1951–1965 and 2003–2010) minus “positive PDO and negative AMO” period

706 (1978–1999). (a) Land precipitation (mm day^{-1}) in CRU TS v3.23. (b) Ensemble mean of ALL run. Only

707 statistically significant anomalies at 95% confidence level are shown. (c) SST (K) in HadISST

708



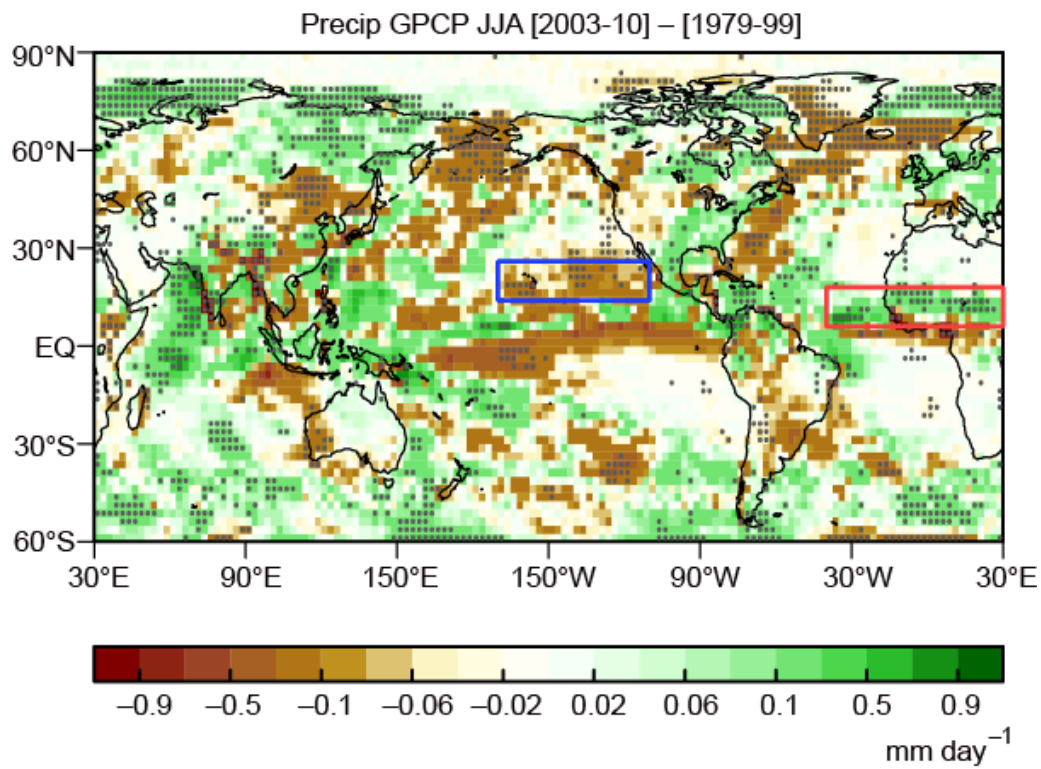
709

710

711 **Fig. 5** Similar to Fig. 4, but for “negative PDO and negative AMO” period (1966–1977) minus “positive PDO

712 and positive AMO” period (2000–2002)

713



714

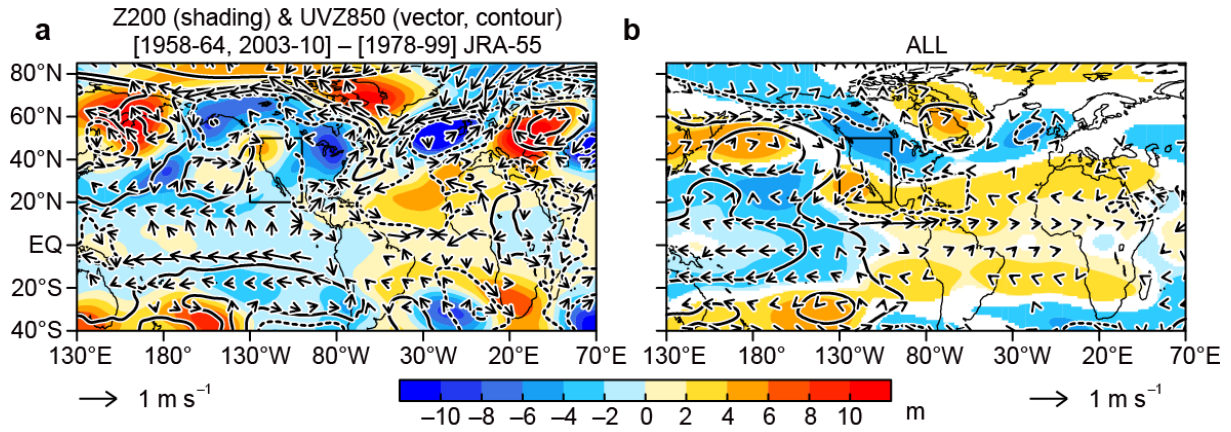
715

716 **Fig. 6** JJA-mean precipitation anomaly (mm day⁻¹) in GPCP during 2003–2010 relative to 1979–1999. Stipples

717 indicate regions with statistically significant anomaly at 95% confidence level. Blue and red rectangles are

718 the eastern tropical Pacific (ePac) and tropical Atlantic (tAtl) regions used in Fig. 8, respectively

719



720

721

722 **Fig. 7** (a) Composite anomalies of JJA-mean atmospheric circulation for “negative PDO and positive AMO”

723 period (1958–1965 and 2003–2010) minus “positive PDO and negative AMO” period (1978–1999) in

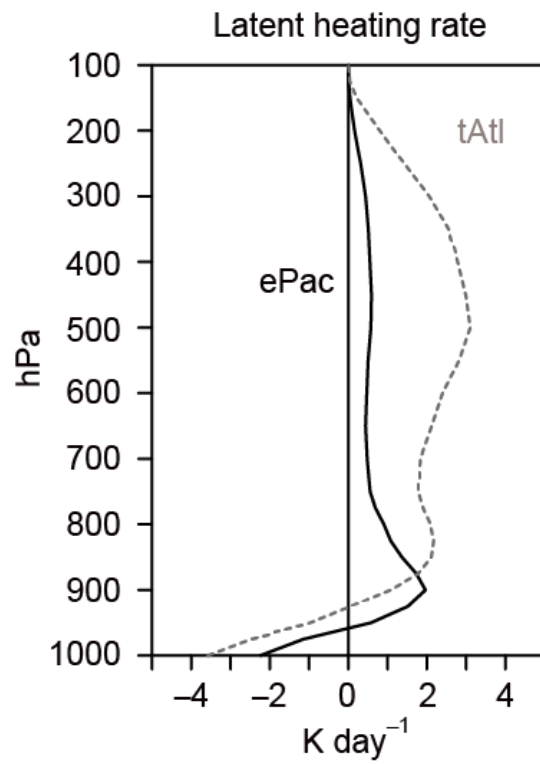
724 JRA-55. Shading represents eddy component (anomaly from zonal mean) of geopotential height (m) at 200

725 hPa level. Vectors and contours are wind (m s^{-1}) and geopotential height ($\pm 1, 3, 10$ m) at 850 hPa level,

726 respectively. Solid and dashed contours represent positive and negative anomalies. (b) Similar to (a) but for

727 the ALL run. Only anomalies with 95% confidence level are shown

728



729

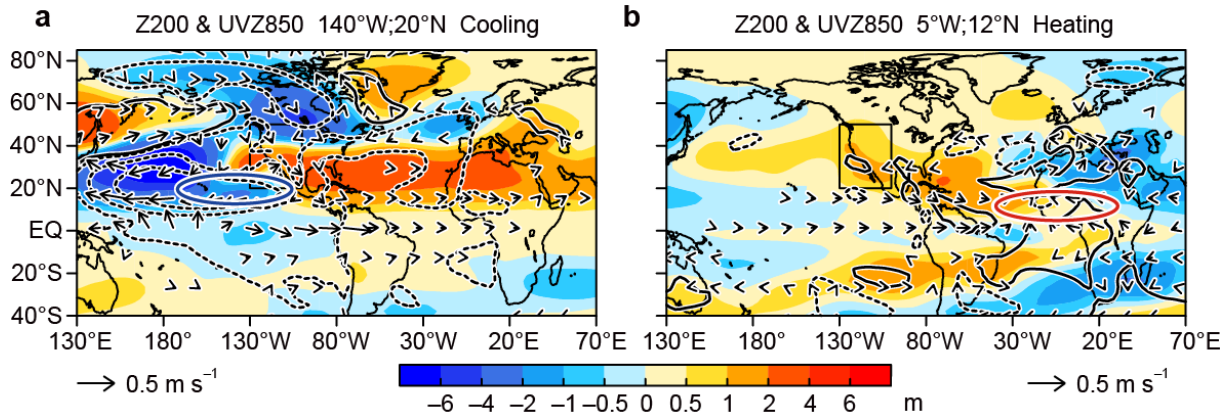
730

731 **Fig. 8** Climatological (1951–2010) atmospheric heating rate (K day⁻¹) due to large-scale condensation and

732 convective precipitation in JRA-55. Black solid and gray dashed lines are averages over the ePac and tAtl

733 regions shown in Fig. 6

734



735

736

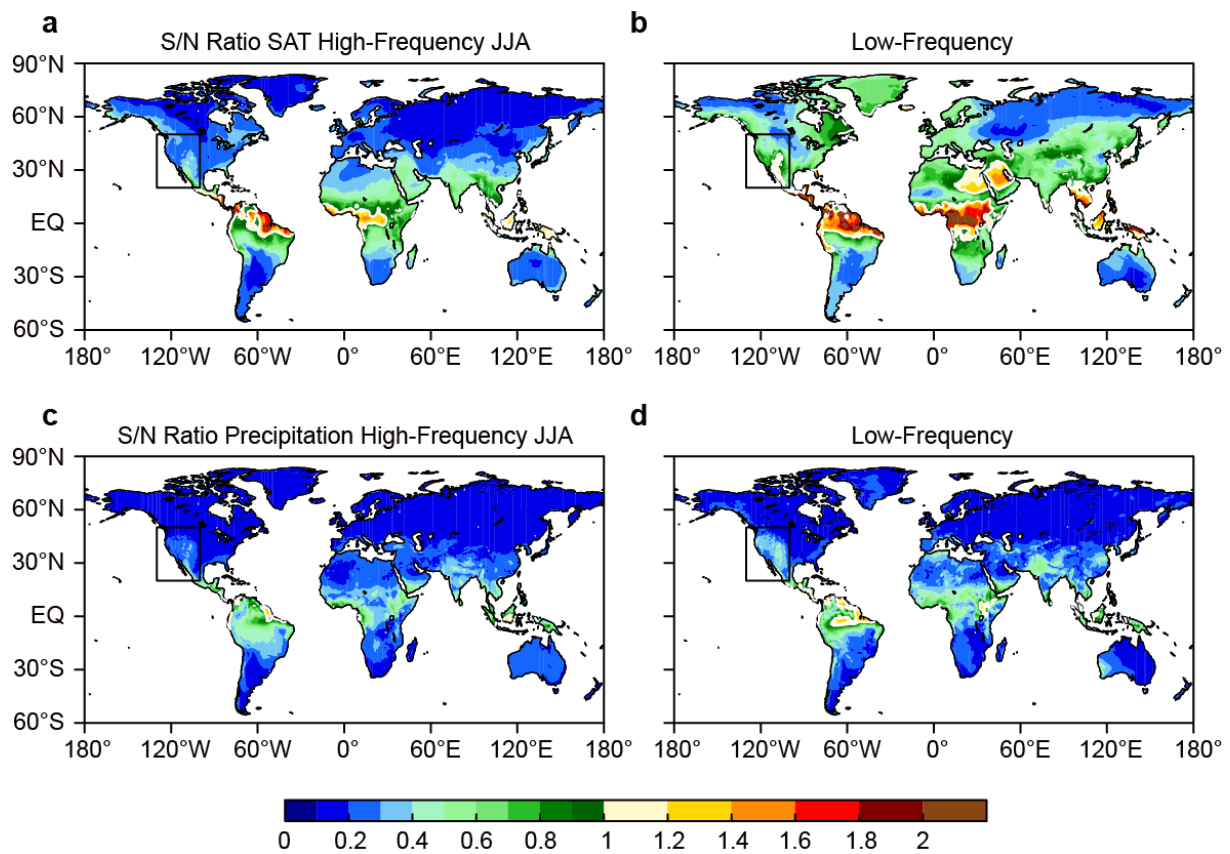
737 **Fig. 9** Similar to Fig. 7, but for atmospheric response to tropical diabatic heating simulated in Linear Baroclinic

738 Model (Sect. 2.3). (a) Atmospheric response to lower-tropospheric cooling over ePac region centered at

739 140°W, 20°N (blue circle). Contours are geopotential height at 850 hPa level ($\pm 0.1, 0.5, 1$ m). (b) Similar to

740 (a) but for middle-tropospheric heating over tAtl region centered at 5°W, 12°N (red circle)

741



742

743

744 **Fig. 10** Signal-to-noise ratio during JJA determined by a ratio of standard deviation in 100-member ensemble

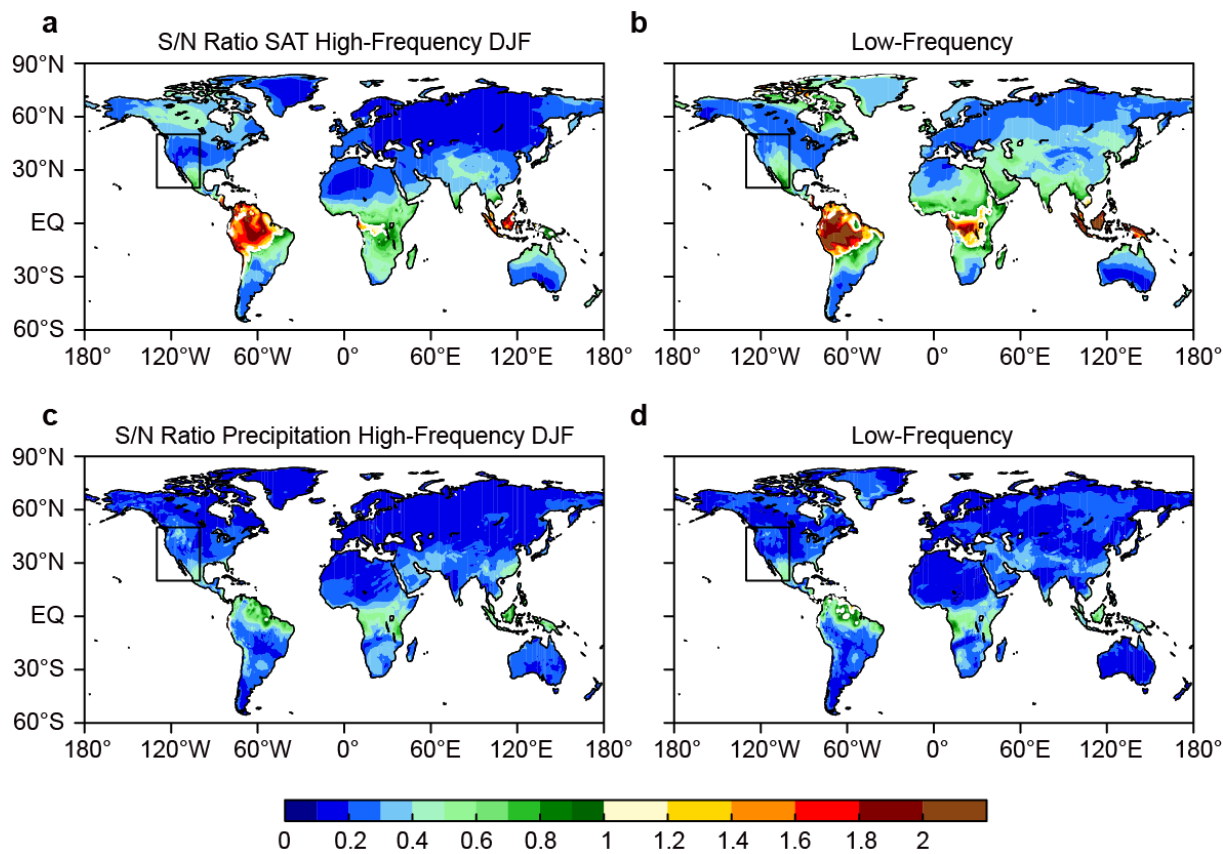
745 mean to standard deviation among the members. (a) High-frequency and (b) low-frequency SAT variation

746 shorter than 15 years and longer than or equal to 15 years, respectively. White contour represents 1.0. (c, d)

747 Similar to (a, b) but for precipitation

748

749



750

751

752 **Fig. 11** Similar to Fig. 10, but for December-January-February (DJF)

753